Figure 2. Environmental conditions of the virtual ecosystem SIVA-T05 are designed to be finite and heterogeneous.
(A) Spatial design. The virtual space of SIVA-T05 is a two-dimensional lattice (B) Spatial distribution of environmental conditions. Left: Distribution of environmental temperature. Initial distribution of energy stocked in each spatial block. Right: Initial distribution of four kinds of virtual inorganic biomaterials (VI). Each substance flows between adjacent spatial blocks to restore the environment to the initial condition when the amount of a substance goes above or below that of the predetermined level.

diffusion and radiation in the terrestrial ecosystem, a predefined amount of energy per time unit is refilled, and the total amount of energy in each spatial block must not exceed a predetermined threshold. The amount of refilled energy and the upper limit of total energy are set at appropriate levels so that a simulation does not become meaningless, that is, not so small that no VLI can live stably and not so large that all VLIs can always live without any failure.

B) Design of Virtual Life in SIVA-T05. In SIVA-T05, we have designed a new type of virtual life based on the hierarchical biomolecular covalent bond (HBCB) model (Oohashi et al. 2009). Table 1 shows the design of the hierarchical structure of virtual biomolecules based on the complexity of the interatomic network of actual biomolecules that compose terrestrial life.

Virtual biological polymers (VPs) and virtual biological monomers (VMs) are categorized into two groups: the functional module group and the constitutive information group, which in terrestrial life correspond to the phenotype and the genotype respectively.

Basically each substance in a certain class consists of several elements belonging to the next lower class. For example, a virtual organic biomaterial (VO) consists of several virtual inorganic biomaterials (VIs), and a VM consists of several VOs. Several VMs constitute a functional unit, which is a subclass of its VP class, and several functional units constitute a larger VP. In the present simulation experiments, we designed five VMs as a single functional unit. A functional unit serves as one word in the SIVA language in the functional module group and also constitutes a virtual codon (Vcodon) in the constitutive information group. Oohashi's SRSD automaton is installed as an artificial life form in SIVA-T05 (Figure 3). The VLI consists of a virtual genome and functional automata. The virtual genome is a VP of the constitutive information group and corresponds to instruction

tape I in Figure 3, whereas the functional automata are VPs belonging to the functional module group and correspond to automata A, B, C, and FZ in Figure 3. The virtual genome encompasses the functions of preservation, replication, and transcription of structural and functional information about a VLI, while the functional automaton encompasses various life activities of the VLI, such as synthesis, decomposition, and reproduction.

The virtual genome consists of a sequence of four kinds of VM (W, X, Y, Z in Table 1) corresponding to the nucleotide in terrestrial life (Figure 3). In the virtual genome, five VMs constitute a functional unit, which serves as a Vcodon. Namely, each Vcodon is defined as corresponding to one of 18 kinds of VM (I, J, K, L; O, P, Q, R; 0–9 in Table 1) of the functional module group (i.e., virtual amino acid: VAA). The sequence of Vcodons defines the sequence of the VAAs in a functional automaton. The sequence information regarding all automata is described in the virtual genome. For the reproduction of a VLI, automaton B replicates the whole virtual genome, and automaton A synthesizes a functional automaton. Mutation can occur in either of these processes.

SIVA-T05 executes the functions of the automata described by the SIVA language as an interpreter by which life activities of VLIs are expressed. First, a functional unit consisting of a sequence of five VAAs serves as a <word> in the SIVA language. A <word> can be categorized as a functional word, which serves as an executable <command>, or as a temporary information word (Table 1). A <command> as a functional word covers a substantial part of the life activities of a VLI. One or more words constitute a <sentence>, which has to include zero or more <command>s and one <period> at the end. Before a <command>, a <sentence> can include one or more conditional phrases. When there is no conditional phrase in the <sentence>, <command>s are directly executed in the order described in the <sentence>. If a <sentence> includes any conditional phrases, a <command> is executed only when

Table1: Hierarchization of virtual biomolecules composing virtual life based on the complexity of the inter-atomic network.

| Class name	Functional module group		Constitutive information group
Virtual biological polymer (VP)	Polymerized functional units		
Functional unit	Functional word (command)	Temporary information word (variable, relational operator etc.)	Virtual codon
Virtual biological monomer (VM)	O P Q R(4 kinds)	I J K L0 1 2 3 4 5 6 7 8 9 (14 kinds)	W X Y Z(4 kinds)
Virtual organic biomaterial (VO)	A B C D (4 kinds/upper-case letter)		
Virtual inorganic biomaterial (VI)	a b c d (4 kinds/lower-case letter)		
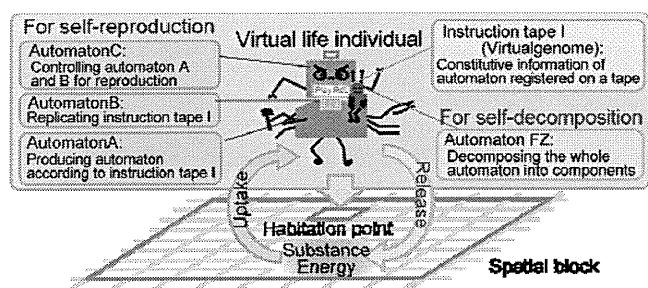
Figure 3. Relationship between life activities of virtual life individuals (VLIs) and the environment in SIVA-T05. Oohashi's SRSD automaton is implemented in the VLI in SIVA-T05. Each VLI consists of functional automata for self-reproduction [D (=A+B+C)], those for self-decomposition [FZ], and an instruction tape [ID+FZ] (i.e., a virtual genome) that is a blueprint of all the automata. Automaton A produces all the functional automata described in the virtual genome. Automaton B replicates the virtual genome. Automaton C constitutes a daughter VLI, combining the automata newly synthesized by automaton A and the virtual genome replicated by automaton B, and divides it from the parental VLI. Automaton FZ decomposes a VLI when the VLI encounters environmental conditions unsuitable for survival or when it lives out its life span. A VLI can reproduce itself by the uptaking of substances and energy existing in the spatial block to which its habitation point belongs. During self-decomposition, the substances and the energy generated by the decomposition of virtual biomolecules constituting the VLI are restored to the spatial block. The occupied space is also released for utilization by another VLI.

all the conditional phrases are true but not when any of the conditional phrases is false. On the basis of these rules, a VLI can be programmed to undergo individual division when all conditions are satisfied, and to decompose itself when unfitness for its environment exceeds threshold level, etc.

Each VLI expresses its life activities by executing all <sentence>s during one time count (TC), the unit of virtual time in SIVA-T05. The order in which a VLI in the virtual ecosystem expresses its life activities within one TC is randomly determined at every TC. It takes at least 5 TCs for a newborn individual to reproduce itself in our current simulation experiments. Therefore, we use <passage duration> as a virtual time unit, which corresponds to the value of TC divided by 5.

When a VLI reproduces itself, it chooses a habitation point for a newborn VLI adjacent to its own habitation point. If the life activities of a newborn VLI fit the environmental conditions in the habitation point, it can also reproduce itself. If such activities do not do so, the newborn VLI decomposes itself prior to reproduction. Since certain mutations may accumulate as generation changes recur, certain offspring may emerge whose life activities fit environmental conditions differing slightly from those existing for their parents. Consequently, VLIs increase or decrease the size of their habitation point. (Oohashi et. al., 2009)

3) Experimental conditions

First, we designed a VLI of a mortal organism with a genetic program for death. This VLI has Automaton A, B, C and FZ as described in Figure 1 and 3, an initialization Automaton that produces the initial setting of the VLI, and a virtual genome corresponding to these Automata. On the basis of the PSD model (see Figure 1), the Automaton FZ, the mechanism for death, was designed to be activated when either of the following conditions is true: (1) unconformity between the VLI and its habitation environment or (2) the end of the life span of the VLI. We took advantage of this mechanism to design a VLI of an immortal organism, of which the value of both the conditional phrases of SIVA language for Automaton FZ were kept unchangeable at a false value and accordingly the functional words in SIVA language for self-decomposition in the FZ automaton were kept unchangeable at an inactivated state. If a mutation occurs in one of these conditional phrases and the value of either conditional phrase becomes changeable, it means that a mortal VLI is evolutionarily born. The functional words in SIVA language for self-decomposition of the mutant VLI will become activated, and the VLI will decompose itself when the above conditions become satisfied during the life of the VLI.

We seeded a single VLI that possessed this precursor of a genetic program for death in the center habitation point of the ecosystem with suitable environmental conditions and then conducted simulations of reproduction and evolution.

In the present simulation experiments, mutation of virtual genomes randomly occurs at the probability predetermined as a mutation rate. We investigated three mutation rates as follows: 0.005, 0.002 and 0.001. Mutation rates of the existing terrestrial lives are distributed from 10-4 to 10-10. There is a tendency for a living organism with a small genome to exhibit a large mutation rate. For example, an organism with a genome of 104 molecules has a 10-4 mutation rate. Virtual genomes of the VLIs in the present simulation experiments consist of 1275 molecules of VM, so we think the above configured mutation rates are within an appropriate range.

Consequently, we conducted 200, 500 and 800 simulations at mutation rates of 0.005, 0.002 and 0.001, respectively. The simulations were of 800 passage durations. Changes in size of the habitation area, number of individuals, and frequency of mutation were observed.

Results

The rates at which mortal organisms evolutionarily emerged and survived are shown in Table 2. The denominators are the number of simulation trials including many cases in which no valid mutation occurred or no VLI of a mortal organism emerged within the 800 passage durations. The rates are 3.5%, 1.4%, and 0.25% for mutation rates of 0.005, 0.002, and 0.001, respectively. That is to say, when the genetic program for death was evolutionarily acquired, the individual possessing the program and its offspring did not always become extinct and survived within a certain probability.

When a VLI of a mortal organism survived, it and its offspring surpassed VLIs of an immortal organism and became prosperous without exception. Figure 4 shows successive changes of VLI distribution, number of
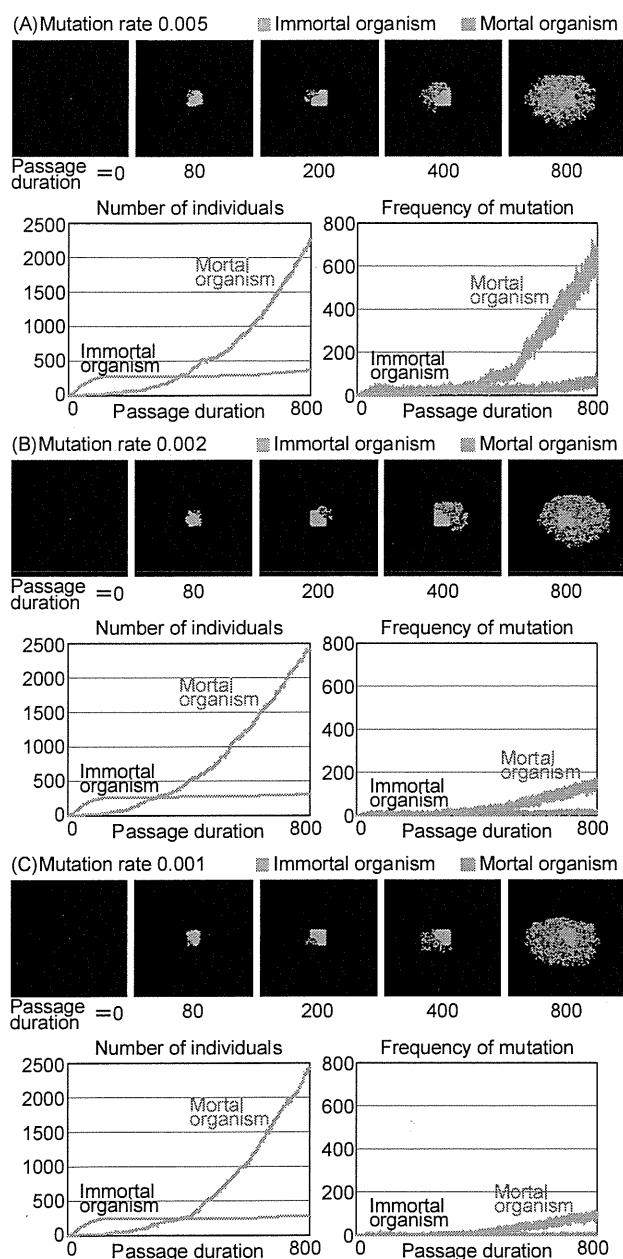
484

(A)Mutation rate 0.005 ▨ Immortal organism ▨ Mortal organism

Passage duration =0   80   200   400   800

Number of individuals

2500
2000
1500
1000
500 Immortal organism   Mortal organism
0
0   Passage duration   800

Frequency of mutation

800
600   Mortal organism
400
200 Immortal organism
0
0   Passage duration   800

(B)Mutation rate 0.002 ▨ Immortal organism ▨ Mortal organism

Passage duration =0   80   200   400   800

Number of individuals

2500
2000
1500
1000
500 Immortal organism   Mortal organism
0
0   Passage duration   800

Frequency of mutation

800
600
400
200   Mortal organism
Immortal organism
0
0   Passage duration   800

(C)Mutation rate 0.001 ▨ Immortal organism ▨ Mortal organism

Passage duration =0   80   200   400   800

Number of individuals

2500
2000
1500
1000
500 Immortal organism   Mortal organism
0
0   Passage duration   800

Frequency of mutation

800
600
400
200   Immortal organism   Mortal organism
0
0   Passage duration   800

Figure 4. Evolutionarily emerging and surviving VLI of mortal organism certainly surpassed VLIs of immortal organism and became prosperous with adaptive divergence under various environmental conditions. Successive changes of individual distribution, the number of individual, and the frequency of mutation were illustrated. (A) 0.005 of mutation rate. (B) 0.002 of mutation rate. (C) 0.001 of mutation rate.

individuals, and frequency of mutation for each mutation rate. For example, for the mutation rate of 0.005 [Figure 4 (A)], a VLI with a genetic program for death emerged at the 30 passage durations' mark and produced offspring without extinction. In the case of 0.002 and 0.001 mutation rates

[Figure 4 (B), (C)], a VLI with a genetic program for death emerged at 11 and 29 passage durations respectively. Both produced offspring without extinction.

Successive changes in the number of individuals and the frequency of mutation shown in Figure 4 demonstrate massive activities of mortal organisms compared to those of immortal organisms. The number of VLIs of a mortal organism grew at a sluggish pace shortly after emergence. However the mortal organisms extended their habitation area by degree, moved ahead of immortal organisms around the 300 or 400 passage duration mark, and then continued to extend their habitation area.

There was no difference observed in the number of VLIs of a mortal organism introduced by the difference in mutation rate. We think the difference in the frequency of mutation of mortal organisms is reasonable because it may be introduced by the difference in mutation rates.

Table2: Probability of evolutionary emergence and survival of mortal organism

Mutation rate	Evolutionary emergence and survival	
	Frequency	Probability
0.005	7 times per 200 trial	3.5%
0.002	7 times per 500 trial	1.4%
0.001	2 times per 800 trial	0.25%

Discussion

1) Mortal organism survived and prospered within a certain probability

We carried out an evolutionary simulation experiment using our artificial ecosystem SIVA-T05, modeled for a finite, heterogeneous terrestrial environment and arranged in a biomolecular hierarchy. In many cases, we observed that when a mortal organism endowed with an evolutionarily acquired genetic program for death was born in a place in which immortal organisms already existed, the mortal organism, instead reproducing, became extinct by means of self-decomposition, overwhelmed by the indigenous immortal organisms.

Nonetheless, our simulation process also demonstrated that some mortal organisms were evolutionarily appeared and managed to survive at a probability of 0.25% to 3.5% in accordance with mutation rates (Table 2). Furthermore, without exception, the mortal organisms that could overcome extinction thereafter prospered to the extent that they surpassed immortal organisms and continued to prosper, thanks to adaptive divergence under various environmental conditions.

Although the probability of the survival and prosperity of the mortal organisms as shown in our simulations was low, it was, nonetheless, significant. Thus we can expect that mortal organisms might evolutionarily emerge, survive and prosper with adaptive divergence in other ecosystems under various environmental conditions while various ecosystems would repeatedly receive not a few opportunities for mutation. Considering the result of the experiment that a 0.25-to-3.5% probability for simulated ecosystems in which mortal

organisms prosper within a short duration of 800 passage durations applied to the terrestrial ecosystem, we believe that scale and heterogeneity of the earth's environment and length of time having elapsed during the evolution of terrestrial life and its concomitant ecosystem constitute sufficient probability for the possibility that mortal organisms could be evolutionarily selected and prosper terrestrially. Hence no inconsistency exists between our results and the experimental results described in our previous report (Oohashi et al. 2001).

2) Explanation of the superiority of mortal organisms

The transition of a number of individual organisms (Figure 4) indicates that the number of mortal organisms surpasses that of immortal organisms at the point in time after which 300-to 400 passage durations has elapsed, and that mortal organisms continue to prosper thereafter. How do mortal organisms overwhelm immortal organisms in this process? One interpretation of this phenomenon is as follows:

Immortal organisms dominate space and materials once they have been secured while the volume of resources to sustain life activities monotonically decreases. With less chance of reproduction in association with decrease of resources, chances for mutation as well as those for evolutionary adaptation are likewise reduced without limit.

On the other hand, mortal organisms release space for other organisms and return optimum parts for them to reutilize through self-decomposition upon termination of their mortal life. By doing so, equally benign or enhanced habitat environmental conditions can thus be secured for the all organisms including their own offspring in the ecosystem, which, in turn, will repeat the alternation of generation by utilizing finite space and materials. It is conceivable that due to accumulated mutations through the alternation of generations, new organisms emerge as a result of accelerated evolutionary adaptation in neighboring areas under environmental conditions that had not previously permitted the existence of earlier generations.

Independent of the studies that we have undertaken since 1987 (Oohashi et. al., 1987, 1996, 1999, 2001, 2009, 2011), Todd implemented artificial death in his ALife system (Todd, 1993, 1994), and those experiments supported the recognition shared with us that death affords another entity its space in which to exist, and that death, accordingly, is essential throughout the ongoing evolutionary process. Nevertheless, the model of death constructed by Todd differs from our model of death in two patently obvious respects. First, death in Todd's model affords no process by which the organism might decompose itself into constituent parts for the efficient and collective reutilization of other organisms, which is an essential feature of our model. Second, the death of an individual in Todd's model appears as a probabilistic phenomenon, or as a given result controlled by the simulation system, in sharp contrast to the activation of death in our model, which is a process genetically regulated in the individual that starts from detection either of the end of its life span or of excess unconformity with the environment. Consequently, it would be difficult to use the ALife system as constructed by Todd to investigate the evolutionary emergence of death itself.

It is noteworthy that the mechanism of programmed self-decomposition, observed as being evolutionarily selected in this study, accords benefits not only to direct offspring but also to all organisms of the entire ecosystem. It is difficult to produce a tenable explanation for this phenomenon based only on the "selfish gene" paradigm.

Programmed self-decomposition has been observed as a life phenomenon of existent terrestrial life as previously reported (Oohashi et al, 1987, 2009). The gradual consolidation of these complementary approaches—ALife simulations and biological experiments—will likely throw added light on this topic in the future.

3) Conclusion

The evolutionary simulations using our artificial ecosystem SIVA-T05 show that, if mortal organisms evolutionarily acquire a genetic program for autonomous death and then appear among a population of immortal organisms, such mortal organisms, endowed as they are with a genetic program for autonomous death, can survive and will surpass immortal organisms lacking autonomous death and will prosper with adaptive divergence under various environmental conditions within a certain probability.

The above results thus support our hypothesis that originally immortal organisms evolve into mortal organisms by acquiring a new genetic program for autonomous death.

References

Odum, E. P. (1971). *Fundamentals of Ecology (3rd ed.)*. Philadelphia, PA: W.B. Saunders Company.

Oohashi, T., Nakata, D., Kikuta, T., and Murakami, K. (1987). Programmed self-decomposition model. *Kagakukisoron (in Japanese)*, 18(2): 21-29.

Oohashi T., Maekawa T., Ueno O., and Honda M. (2011). The supremacy of the altruistic gene: Terrestrial life has succeeded in breaking through evolutionary deadlock. *Kagaku (in Japanese)*, 81(1):83-90.

Oohashi, T., Maekawa, T., Ueno, O., Kawai, N., Nishina, E., and Shimohara, K. (2001). Artificial life based on the programmed self-decomposition model: SIVA. *Journal of Artificial Life and Robotics*, 5(2):77-87.

Oohashi, T., Maekawa, T., Ueno, O., Nishina, E., Kawai, N. (1999). Requirements for immortal ALife to exterminate mortal ALife in one finite, heterogeneous ecosystem, *Proceedings of the 5th European Conference on Artificial Life*, pages 49-53. Springer-Verlag, London, UK.

Oohashi, T., Sayama, H., Ueno, O., and Maekawa, T. (1996). Artificial life based on programmed self-decomposition model. *ATR Technical Report*, TR-H-198.

Oohashi T., Ueno O., Maekawa T., Kawai N., Nishina E., and Honda M.(2009). An Effective hierarchical model for the biomolecular covalent bond: An approach integrating artificial chemistry and an actual terrestrial life system. Artificial Chemistry Special Issue of Artificial Life, 15(1):29-58.

Suzuki, H. (2004). Network artificial chemistry - Molecular interaction represented by a graph. In M. Bedau, P. Husbands, T. Hutton, S. Kumar & H. Suzuki (Eds.), *Proceedings of Ninth International Conference on the Simulation and Synthesis of Living Systems (ALIFE9) Workshop and Tutorial* (pp. 63-70), Boston, MA.

Todd, P. M. (1993). Artificial Death. *Second European Conference on Artificial Life (ECAL93)*, pages 1048-1059.

Todd, P. M. (1994). Artificial Death. In C. Schneider (Ed.), *Jahresring 41*, pages 90-107. Verlag Silke Schreiber, Munich.

Von Neumann, J. (1951). The general and logical theory of automata. In L. A. Jeffress (Ed.), *Cerebral mechanisms in behavior - The Hixon symposium*. pages. 1-41, John Wiley & Sons, New York.

衛生・公衆衛生学

編著者	山本　玲子
著者	上原　鳴夫
	亀尾　聡美
	小松　正子
	金野　吉光
	関田　康慶
	高橋　弘彦
	千葉　啓子
	土井　　豊
	西郡　光昭
	吉田寿美子

第6章　主要疾患の疫学と予防対策

第7章　保健・医療・福祉・介護制度とシステム

目的で**検疫法**に基づいて検疫が行われている。1類感染症の他，4類のデング熱，マラリア，新型インフルエンザ等感染症(豚インフルエンザ)，2類の鳥インフルエンザ(H5N1)，チクングニア熱(2011年2月追加)が**検疫感染症**に指定されている。

〈山本玲子〉

8 精神疾患

厚生労働省の2008(平成20)年の調査では，精神疾患の患者は323万人にのぼり，237万人の糖尿病，152万人のがんなど他の4大疾病を大幅に上回った。このような精神疾患の増加を受け同省は2011(平成23)年7月6日，精神疾患を，がん，脳卒中，急性心筋梗塞，糖尿病と並ぶ「5大疾患」と位置づけ，重点的対策を行う方針を示した。

8-1 統合失調症(精神分裂病，シゾフレニア(schizophrenia))

以前 schizophrenia は「精神分裂病」と和訳されていた。この診断名はまるで「精神が分裂している病で，何をするかわからない恐ろしい病気」といった暗いイメージを一般の人に与えていたため，実際は回復可能な病気にも関わらず，患者や家族は偏見に基づく苦痛を強いられていた。また，病名に悪いイメージがあるため精神科医も病名告知をためらいがちとなっていた。そのため患者は自分の病名を知らずに治療を継続する困難さを感じ，利用可能な福祉サービスにも無頓着となっていた。そこで，2002(平成14)年に，日本精神神経学会において，本疾患の日本語の呼称を「**統合失調症**」と変更することが決定された。現在では，厚生労働省の諸手続きもこの病名の使用が定着している。

わが国における一般人口中における出現頻度(発生率または罹患危険率)は0.7％前後と高く，**精神病院入院患者**の60～70％を占めている。この出現頻度は洋の東西を問わずほぼ一致している。発生率には性差がなく，10代後半～30歳代に発症することが多い。成因は不明であるが，病的素因，または中枢神経系の脆弱性があり，これが環境因(心因)を誘因として症状を形成する(**脆弱性・ストレスモデル**)との考え方が有力である。最近，症状は**陽性症状**，**陰性症状**，**認知障害**の3つに大別されている。

陽性症状は被害妄想や幻視，幻聴といった症状で，一般の人には基本的には体験できない。陰性症状は意欲の減退や喜怒哀楽の感情が乏しくなるなど，一般の人が本来もっている基本的な精神活動が減退するものである。認知の障害としては注意障害，記憶の障害，概念形成障害などが認められる。

現在では，特に薬物療法の進歩により，入院期間が短縮し，60％以上の患者が寛解，不完全寛解に至っている。しかしながら，服薬継続下の寛解であるため，服薬を中止すると社会的ストレスなどのために容易に再発する。このように退院と再発後の再入院を繰り返す現象は回転ドア現象とよばれ，薬物療法の効果への過信を戒めると共に，精神福祉の重要性を強調するものである。

8-2 気分障害(躁うつ病, うつ病性障害)

気分障害は統合失調症と並ぶ内因性精神病の1つとされていた。しかし，最近はできるだけ症状に基づいた分類を行うという方針から，内因性等の区別無く診断されるようになった。近年のうつ病増加の原因の1つに診断基準の変化もあると考えられている。DSM－Ⅳ－TR(アメリカ精神医学会，精神科疾患の診断・統計マニュアル第4版TR)では**気分障害を双極性障害とうつ病性障害**(以下うつ病と略)**に大別している。双極性障害**は躁病(気分の高揚と活力および活動性の増加)とうつ病(気分の低下と活力および活動性の減少)のエピソードが反復するものである。**生涯有病率**は，日本では双極性障害0.4～1％，うつ病(非双極性)は双極性障害よりも多く1.3～17.8％と推定されている。うつ病は2：1の割合で女性に多く，年齢的には思春期，青年期に多い。具体的な症状としては，抑うつ気分，気力の低下，興味・関心の喪失，注意・思考力の低下，易疲労感，不眠，食欲・性欲の減退を訴えることが多い。治療は患者に強い希死念慮(具体的な自殺方法を考えている)がある場合を除いて外来で行われることが多い。薬物療法と精神療法の1つである認知行動療法が効果的で，ほとんどの患者は完全寛解し，予後は一般に良好である。

うつ病で問題となっているのは，

① 地域社会にいるうつ病者のうち，医師を訪れるのはわずかで，その中でも専門の精神科医を訪れる患者はさらに少ない(**氷山現象**)こと。

② 子供には，うつ病はないとの思い込みから**小・中学生のうつ病**が見逃されていることである。最近の報告によると，100人のうち小学生は1～2人が，中学生は4～5人が「うつ病」の可能性があるという(傳田，2002)。

③ 従来では適応障害と診断されていたと思われる自ら「うつ病」と訴えるうつ病(未熟型うつ病，回避型うつ病，逃避型うつ病：広瀬哲也など)が増加している。抗うつ薬は余り効果がなく，精神療法に導く事も困難なケースが多い。

うつ病は出現頻度がかなり高く，経過も長いので，これが人類の健康に及ぼす影響の大きさが注目されている。世界保健機関WHOは疾病や傷害が世界人類の健康に及ぼす負担(the global burden of disease; GBD)を計算し，2020年には，うつ病性障害が虚血性心疾患に次いで負担になるだろうと予測している。日本では中高年の自殺が増加し，自殺の背景としても注目されている。

8-3 てんかん

種々の原因によって起こる慢性の脳障害で，脳の全体か一部における過剰な電気的活動によって引き起こされる。過剰な電気的活動の出現部位や広がり方に従って，意識障害，けいれん，自動症，流涎などの自律神経症状その他のさまざまな発作を引き起こす。てんかんの出現率は0.3％程度で，総患者数は27.3万人[2005(平成17)年患者調査]と推定されている。てんかんはてんかん国際分類では，脳の障害部位により局在関連てんかんおよび症候群と全般てんかんおよび症候群に大別され，それぞれに特発性(素因以外に原因が明らかでないもの)と症候性(出産時の脳障害，頭部外傷な

ど原因が明らかなもの)に分類されている。特殊なてんかんに点滅光，赤色光，コントラストの強い図形などで誘発される**光過敏てんかん**がある。テレビのアニメーション(たとえばポケットモンスター)でも引き起こされる危険性があり注意を要する。

　てんかんは自然治癒率が2〜10％といわれ，薬物療法や外科手術等でのけいれん発作の完全抑制率は60％程度と発作の予後は改善している。しかしながら，てんかんをもつ個人は，そのスティグマ(偏見に基づくいわれのない汚名)から結婚，就職，スポーツ，車の運転など通常の活動に参加する機会を奪われているという現状がある。

8-4　知的障害

　知的障害とは，精神の発達停止，または発達不全の状態であり，認知，言語，運動および社会的能力など全体的な知能の障害が，発達期(18歳未満)に明らかになるものである。知的障害の全体的有病率は1〜3％と推定されている。知的障害の原因は原因が個体に働いた時期により先天性(出生前)と後天性(周産期・出生後)に分類され，いずれも脳に何らかの障害を引き起こすことが多い。WHOは知能指数IQにより，軽度(50〜69；精神年齢9〜12歳)，中等度(35〜49；精神年齢6〜9歳)，重度(20〜34；精神年齢3〜6歳)，最重度(0〜19；精神年齢3歳以下)と分類している。知的障害をもたらす代表的な疾患はダウン症候群である。**ダウン症候群**は染色体異常によって引き起こされ，**21トリソミー**(21番染色体が3個存在する)が最も多い。先天性代謝異常など適切な医学的処置によって予防できる知的障害もある。

8-5　精神作用薬物使用による精神および行動障害(薬物依存)

　精神作用物質使用による精神障害および行動の障害には，アルコール，アヘン類，マリファナのような大麻類，鎮痛剤や催眠剤，コカインや他の覚せい剤，たばこや揮発性溶剤などの使用により起こる障害が含まれる。その状態は，中毒，有害な使用，依存症や精神病性障害を含んでいる。有害な使用とは，身体あるいは精神面の健康に害を及ぼすときに使用される。依存は「薬物の使用による快楽を得るため，あるいは離脱による不快を避けるために，有害であることを知りながらその薬物を続けて使用せずにはいられなくなった状態」をさし，薬物の反復摂取は報酬系(刺激により快感を生じる脳の回路)を中心とした脳の機能変化を引き起こすと考えられている。

　世界的に最も広く使用されている**精神作用薬物**は，たばことアルコールであるが，これらについては他項(第5章5, 6：喫煙・飲酒，p.71〜74)を参照されたい。わが国では，**覚せい剤**と**有機溶剤**の乱用が多く，特に覚せい剤は1995年から第3次乱用期に入っている。これは，一部外国人による密売の増加，乱用の低年齢化，インターネットなど新しい通信技術の悪用などの特徴をもち，対策が困難となっている。また，覚せい剤は単に依存を形成するだけでなく，統合失調症に近似した症状をもつ**覚せい剤精神病**を引き起こす危険性があるので，特に注意が必要である。精神作用薬物は覚せい剤取締法などの法律によって厳しい規制が行われているが，最近は"合法ドラッグ(法の規制を受けていない薬物；マジックマッシュルームなど)"が簡単に入手でき，

若者を中心に乱用が増加し，社会問題となっている。

8-6　心的外傷後ストレス障害（post-traumaticstress disorder; PTSD）

　自然災害，大事故，テロ等の例外的に著しく脅威的あるいは破壊的な性質をもったストレスが心的外傷となり，遅延または遷延した反応として現れる。日本では，阪神・淡路大震災でその存在を注目されてから，一般的となった。典型的な症状は無感覚と感情鈍化，外傷を思い出させる状況を避けているのに，ストレスとなった場面が無意識に思い出されるフラッシュバック，夢の中で繰り返される外傷の再体験である。時に強い恐怖感，パニック，攻撃性が急激に生じることがある。強い驚愕反応，不眠，不安，抑うつを伴い自殺念慮を伴うこともある。

8-7　認知症（痴呆）

　認知症は，いったん正常に発達した知能が後天的な脳の器質的障害により低下した状態をさす。認知症は脳血管性と変性性に大別され，変性性認知症としてはアルツハイマー型が最も多い。認知症は記憶障害，見当識障害（場所や時間などがわからない），判断障害を基本障害とし，不適切な感情，人格の変化を伴う。時に幻覚や妄想などの行動障害を伴うが必須ではない。日本では脳血管性認知症が多かったが，人口の高齢化に伴いアルツハイマー型認知症が増加している。アルツハイマー型認知症の有病率は1〜5％と幅が広い。これは年齢が進むにつれて発現は急速に増加する（おおよそ5年ごとに倍加する）ためである。アルツハイマー型認知症の原因は代謝異常，アミロイド類前駆物質タンパク，プラーク関連タンパク，タウタンパク，亜鉛やアルミニウム等の代謝障害，アポリポタンパクの遺伝子多型の違いなど発症リスクを高める遺伝子などが示唆されているが，依然不明である。脳血管性認知症を予防するには，その原因となる生活習慣病を予防することが重要である。アルツハイマー型認知症の予防については不明であるが，廃用性による脳の機能低下を防ぐために，計算や運動など頭や体を使うことが有用とされている。またアルツハイマー型認知症にはドネペジル（商品名：アリセプト），メマンチン（商品名：メマリー），ガランタミン（商品名：レミニール），リバスチグミン（商品名：イクセロンパッチ，リバスタッチ）などが症状緩和や進行の緩徐化に効果を発揮することがある。またアルツハイマー型認知症のワクチンも開発されつつある。

　日本では2004（平成16）年12月24日付けで，関連各学会においても2007（平成19）年までに痴呆の呼称が行政上「認知症」となった。

９　自　殺

　自殺は世界的には15〜34歳の年齢群で死亡原因の上位3位にあり，世界公衆衛生上の重大な問題となっている。自殺率は10万人につき15.1人とされ，老年期を除き圧倒的に男性が多い（男：女　3.5：1）。日本では，警察庁生活安全局の報告によると，

中高年の自殺の増加に伴い，2003（平成15）年の自殺既遂者は3万4千人を越え，以後3万2～3千人前後で推移している。自殺未遂者は自殺既遂者の20倍以上になるといわれ，日本でも大きな社会問題となっている。同局の報告によると2003年度の自殺の原因・動機としては，「健康問題」が最も多く，「経済・生活問題」，「家庭問題」がこれに続いている。精神障害による自殺のなかでは，うつ病が最も多く（Pokorny, 1964），その自殺は反復される傾向がある。先に述べた，統合失調症，精神作用薬物使用による精神および行動障害やPTSDも原因となり得る（表5-17, 別冊 p.18）。

　自殺予防の1つとして，自殺の危険性が高い精神疾患であるうつ病の有無を明らかにして，治療に結びつけることが挙げられる。うつ病は治る病気であることから，家族や職場でうつ病に関する教育を行い，うつ病の場合には早急に治療を受けさせるようにすることが重要である。「仕事の失敗から」，「借金を苦にして」，「人間関係に疲れて」などによるとされる自殺のかなりの部分は，適切な医療を受ければ治癒し得るうつ病によるものと考えられている。老年期の自殺予防には孤独感や疎外感をもたせないこと，何らかの役割を持たせることが有効とされている。また，一度自殺企図を行った人は，繰り返す傾向があるので充分な注意が必要である（一度自殺を図って助かった人は二度と自殺しないというのは間違いである）。

〈吉田寿美子〉

10　その他の疾患

10-1　肝臓疾患

　肝臓疾患の主要なものに肝硬変が挙げられる。肝硬変は肝細胞の壊死を伴う肝機能不全状態である。成因の大半をウイルス性肝炎が占め（C型肝炎約60％，B型肝炎約15％），アルコール性が1割強である。

　ウイルス肝炎には，A型，B型，C型，D型，E型の5種類が確認されている。A型肝炎は食物（生牡蠣など魚介類）・飲料水等からの経口感染により平均約30日の潜伏期ののち急激に発症するが，慢性化せず予後良好である。症状は，発熱，悪心・嘔吐，腹痛，全身倦怠感，黄疸などである。

　B型肝炎は血液，唾液などを通して感染し，乳幼児が感染した場合は持続感染者（キャリア）となりやすいが，成人が感染した場合慢性化することはまれとされる。かつては出産時における母子感染等が多かったこともあり，B型肝炎ウイルスキャリアは推定110～140万人いるが，昭和60年度から妊婦検診でHBs抗原検査を行い，子に対するワクチン投与などの適切な予防措置を講じたため（B型肝炎母子感染防止事業），キャリアの数は減少している。

　一方，C型肝炎は血液により感染し（輸血，入れ墨，注射器等），感染年齢にかかわらず高率に慢性化しキャリアとなる。日本には推定200～240万人のキャリアがおり，そのうち一定の割合（6割という推定もある）が20年をかけて肝硬変に移行し，さらに肝がんへと移行する。したがって，C型慢性肝炎患者にはインターフェロンやリバビリン，ペグインターフェロンによりウイルスを駆除する治療等が必要となる。感染予

Development of a Brain PET System, PET-Hat: A Wearable PET System for Brain Research

Seiichi Yamamoto, *Member, IEEE*, Manabu Honda, Tutomu Oohashi, Keiji Shimizu, and Michio Senda

Abstract—Brain functional studies using PET have advantages over fMRI in some areas such as auditory research in part because PET systems produce no acoustic noise during acquisition. However commercially available PET systems are designed for whole body studies and are not optimized for brain functional studies. We developed a low cost, small, wearable brain PET system named PET-Hat dedicated for brain imaging. It employs double counter-balanced systems for mechanical supports of the detector ring while allowing the subject some freedom of motion. The motion enables subject to be measured in the sitting position and move relatively freely with the PET during acquisition. The detector consists of a Gd_2SiO_5 (GSO) block, a tapered light guide and a flat panel photomultiplier tube (FP-PMT). Two types of GSO are used for depth-of-interaction (DOI) separation allowing the use of a small ring diameter without resolution degradation. The tapered light guide allows the use of larger GSO blocks with fewer FP-PMTs. Sixteen detector blocks are arranged in a 280 mm diameter ring. Transaxial and axial field-of-view (FOV) are 20 cm and 4.8 cm, respectively. Energy resolution of the block detectors was $\sim$ 15% full width at half maximum (FWHM) and timing resolution was $\sim$ 4.6 ns FWHM. Transaxial resolution and axial resolution at the center of the FOV were $\sim$ 4.0 mm FWHM and $\sim$ 3.5 mm FWHM, respectively. Sensitivity was 0.7% at the center of the axial FOV. Scatter fraction was $\sim$ 0.6. Hoffman brain phantom images were successfully obtained. We conclude that the PET-Hat is a promising, low cost, small, wearable brain PET system for brain functional studies.

Index Terms—Brain, GSO, PET, PSPMT, wearable.

I. INTRODUCTION

IN the early stage of human activation studies, positron emission tomography (PET) was used and many interesting brain functional insights were obtained [1]–[4]. After the introduction of the functional magnetic resonance imaging (fMRI) [5]–[6], most of these brain functional studies were shifted from PET to fMRI because the latter does not require positron radionuclides and thus does not require injections and has no radiation exposure. Furthermore, the activation sensitivity to the stimulation is generally higher than PET.

One drawback of the fMRI studies is the acoustic noise from the gradient sequence which makes it difficult to use for auditory experiments in human studies. Acoustic noise in MRI is usually more than 100 dB sound presser level (SPL) requiring headphones or bone conduction speakers for the auditory stimulation for fMRI studies, making it quite different from natural auditory conditions

Another drawback of the fMRI studies is that subject needs to lie in narrow and deep tunnel of the MRI making most of subjects uneasy, especially for subjects of claustrophobic show difficulty in measuring in MRI [7] and [8].

Brain functional studies using PET have advantages over fMRI in some areas such as auditory research of the brain because recent PET systems basically produce no acoustic noise with acquisition. However commercially available PET systems are designed for whole body studies and are not optimized for brain functional studies. Most of the commercial available PET systems are for imaging human body thus the diameter of the detector ring is large enough to image the human whole body increasing the cost and reducing the sensitivity of the PET system [9]–[12]. In addition, these commercially available PET systems measure subject lying on the bed in the tunnel of the PET. In the case of PET/CT system, the length of the tunnel became longer [9], [11] and the similar drawback to MRI system may be serious for claustrophobic subjects.

In the brain functional studies using delicate auditory stimulation, fMRI may not be a candidate for the imaging modality because of the serious acoustic noises and narrow spaces in the MRI measurements. PET will have an advantage for these applications. Commercially available whole-body PET systems are better, but like the MRI, subjects are measured while lying on the bed in the relatively long tunnel. In addition, the acoustic noise level in the tunnels of PET systems is much smaller than in MRI but relatively high from such as the cooling fans of the electronics in the gantry of the system.

For the measurements of sensitive stimulation such as the detection of hypersonic effect [13], subject must be measured in a silent and relaxed condition where the only target stimulus activates the subject. For the relax condition, it will be better to be measured in the sitting position. And if the detector ring can move with the subject's head, the subject may feel more relaxed during PET measurement while minimizing the head movement.

Some PET systems dedicated for brain measurements have been developed [14]–[18]. However in most of the PET system, subject must be lying on the bed during measurement while one

Fig. 1. Conceptual drawing of the PET-Hat.

Fig. 2. Photograph of GSO block detector (from the top, GSO block, tapered light guide and FP-PMT) used for the PET-Hat. In photograph, printed boards of weighted summing amplifiers are shown under FP-PMT.
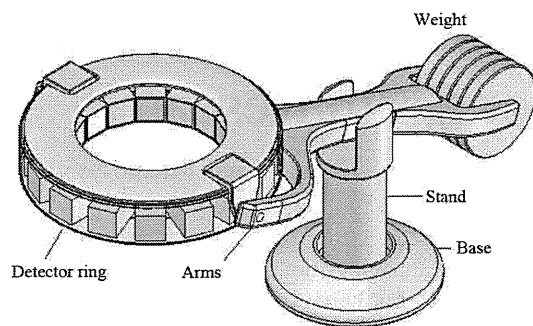
of the PET systems can measure in the sitting or standing position [18] but subject cannot move freely during measurement with the PET system. If the subject can move relatively freely while measurement, new neurological data that are impossible to measure such as measurements of blood flow changes during body or heads movement may become possible. Trying to satisfy these demands on the PET brain studies, we have developed a low cost, small and wearable PET system named PET-Hat.

II. MATERIALS AND METHODS

A. Conceptual Design of the PET-Hat

Fig. 1 shows the conceptual drawing of the PET-Hat. The PET-Hat employs double counter-balanced systems in the mechanical supports. The detector ring of the PET system is supported by arms around which the detector ring can freely rotate during acquisition because the detector ring is balanced in the arms. The arms are supported by a stand and the detector weight is counterbalanced, which allows flee up and down motion. In addition, the stand can freely rotate around the base of the stand. These three motions enable subject to move relatively freely with the PET detector ring during acquisition by softly connecting the detector ring with the subject head.

B. GSO DOI Detector Block of the PET-Hat

The block detector for the PET-Hat consists of a Gd_2SiO_5 (GSO) block, a tapered light guide and a flat panel photomultiplier tube (FP-PMT). GSO was selected for the scintillators because the decay times can be controlled by the Ce concentration. Two types of GSO are stacked in the depth direction to form the depth-of-interaction (DOI) detector [19] and [20]. The DOI detection makes it possible to minimize the ring diameter of the PET system because it can reduce the spatial resolution degradation at off-center of the field of view (FOV). The tapered light guide is used to increase the size of the GSO blocks and reduce the number of FP-PMTs used for the PET-Hat.

The sizes of the GSO scintillators are 4.9 mm × 5.9 mm × 7 mm for inner layer (GSO with 1.5 mol% Ce: decay time of 40 ns) and 4.9 mm × 5.9 mm × 8 mm for outer layer (GSO with 0.4 mol% Ce: decay time of 80 ns), respectively. The inner layer means the layer closer to subject and the outer closer to the PSPMTs Light output difference between these two types of GSO were within 5%.

Depth length of these GSO scintillators was reduced to minimize the weight of the block detector for increasing the safety
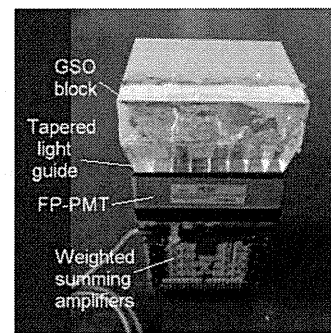
and decreasing the inertia of the PET-Hat. These GSO scintillators are combined into 11 × 8 matrix to form a block with size 55 mm (transaxial) × 48 mm (axial) . The GSO block is optically coupled to a FP-PMT through the tapered light guide. For the FP-PMTs, Hamamatsu H8500, 2-inches 8 × 8 multi-anode type [21] were used. The tapered light guide has 48 mm × 48 mm area in the bottom (near to the FP-PMT) surface and 55 mm × 48 mm in the top (near to the GSO block) surface and 8 × 8 tapered cells are combined with multi-layer optical film (ESR: 3M) between them. Fig. 2 shows the assembled GSO block detector with GSO block, tapered light guide and FP-PMT.

C. Configuration of PET-Hat

Sixteen GSO DOI block detector was arranged in a ring with diameter 280 mm. The signals from each GSO block detector is weighted summed and is fed to 100 MHz analog to digital (A-D) converters of the data acquisition system [22] and signals are integrated with two different integration time (120 ns and 320 ns) [23], calculating the position using the Anger principle by field programmable gate array (FPGA). Also coincidences are measured digitally among eight groups (2 block detectors for 1 group) and stored in list mode to the personal computer (PC). The data acquisition system is basically the same as that used for small animal PET systems [22]. Time window was set to 16 ns and lower energy window to 350 keV. The gain of the FP-PMTs was manually tuned to be similar level before acquiring the position map of the block detectors for setting the position boundaries and energy windows. Data for normalization was measured using a 24 cm diameter ring source phantom containing F-18 solution.

Fig. 3 shows the developed PET-Hat system. It consists of a detector ring with double counter balanced arm, reclining chair and a notebook PC. End-shields made of two layers of 2 mm thick tungsten contained rubber were pasted at the lower edge of the detector ring. The end-shield covered scintillator blocks and the length was 2 cm.

The data acquisition system is encased under the detector ring. The control of the PET-Hat as well as data processing including image reconstruction is controlled by the notebook PC by wireless communication with a desk-top PC under the detector ring.

Fig. 4 shows photograph of the PET-Hat with a subject. Subject can sit on the reclining chair and the PET-Hat can be set
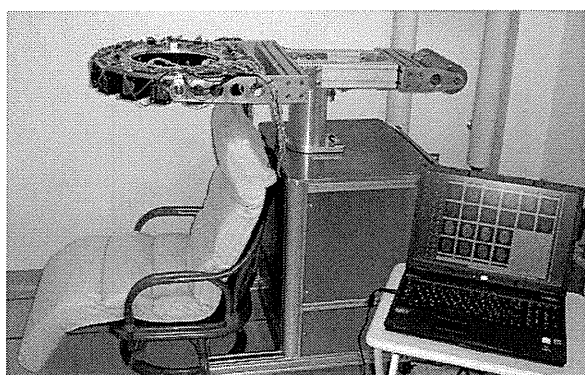
Fig. 3. Developed PET-Hat system.

Fig. 4. PET-Hat system with subject; front view (left) and side view (right).

from the top. By softly connecting the subject's head to detector ring using such as a straw hat that is attached at the detector ring of the PET-Hat, the subject can move relatively freely with the detector ring of the PET-Hat during acquisition.

Parts of a movie showing the movement of the PET-Hat with subject are shown in Fig. 5. The horizontal movement of the head and detector ring of the PET-Hat is shown in Fig. 5(a), the vertical movement in Fig. 5(b). The subject and the detector ring were connected with a straw hat that was connected with the detector ring of the PET-Hat.

D. Performance Evaluation of PET-Hat

1) Spatial Resolution: Spatial resolution measurements were made using a 1 mm diameter spherical shape Na-22 point source (radioactivity: 300 kBq) positioned at the center, 0 cm, 4 cm, 6 cm and 8 cm from the center of the FOV. Random coincidences were subtracted using the delayed data. At each position, more than 100 k counts were accumulated. List mode data were sorted into sinograms, after single slice rebinning with maximum ring difference of 4 and 2D filtered back-projection with ramp equivalent real space filter was used for reconstruction. Images were made with and without DOI correction.

2) Axial Resolution: Axial resolution was measured using the same Na-22 point source (1 mm diameter spherical shape point source, with radioactivity of 300 kBq). Images of the point source were reconstructed using 2D filtered back-projection with ramp equivalent real space filter and coronal images were re-sliced and evaluated.

3) Sensitivity: Sensitivity was measured by moving a Na-22 point source (1 mm diameter spherical shape point source, with

(a)   (b)

Fig. 5. Parts of a movie showing movement of the PET-Hat with subject; horizontal movement (a) and vertical movement (b).

radioactivity of 300 kBq) in the axial direction and true coincidence rates were measured as a function of axial position.

4) Scatter Fraction: Scatter fraction was measured using a National Electrical Manufacturers Association (NEMA) 20 diameter, 70 cm long phantom using F-18 solution (radioactivity: $\sim$ 10 MBq) contained in the tube. The phantom was positioned at the center of the FOV. Scatter fraction was evaluated inside the FOV (20 cm). Scatter fraction was evaluated based on the NEMA NU 2001 standard [24].

5) Count Rate Performance: Count rate performance was measured using a NEMA standard 20 cm diameter, 70 cm height phantom contained $\sim$ 74 MBq F-18 solution. Following the decay of F-18, prompt, delayed and prompt minus delayed count rate were measured.

Noise equivalent count rate was also evaluated using the following formula with k = 2 because we used delayed coincidence for random correction.

$$\text{NECR} = \frac{(T \times T)}{(T + kR + S)}$$

where

T   true count rate

R   random rate

k   Delayed coincidence fraction

S   scatter rate

6) Hoffman Brain Phantom Imaging: The Hoffman brain phantom [25] contained 20 MBq of F-18 solution was positioned at the center of the FOV of the PET-Hat and measurements were made for 2 hours and total counts of $\sim$ 50 Mc were acquired. Data were reconstructed by 2D filtered back-projection using the normalization data. Analytical correction and single value subtraction were used for attenuation correction and scatter correction, respectively.

(a)

Energy(key)

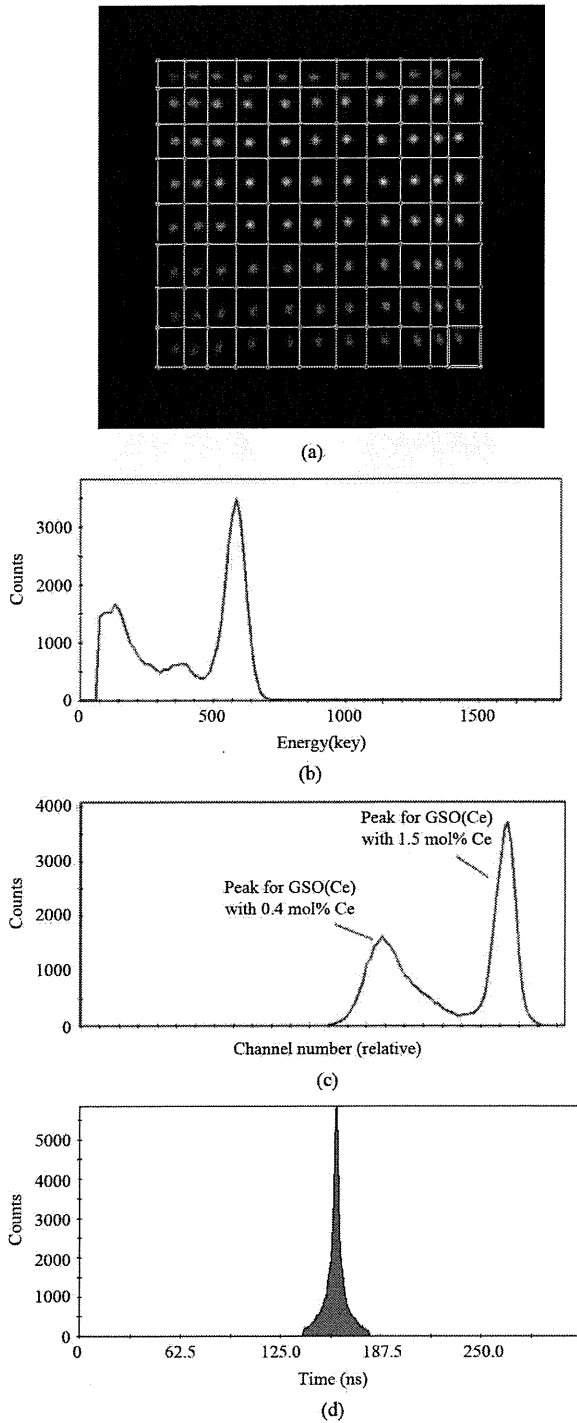(b)

Channel number (relative)

(c)

Time (ns)

(d)

Fig. 6. Position map of the GSO block detector with position boundary (a) energy spectrum (b) pulse shape spectrum (c) and timing spectrum (d) of the GSO DOI block detector.

III. RESULTS

A. Performance of the GSO DOI Block Detector

Fig. 6(a) shows the position map of the GSO block detector. Gamma photons form Cs-137 (661-keV) were irradiated from ∼ 5 cm from the top of the GSO DOI block detector. The position map showed clear separation of all the GSO scintillators.

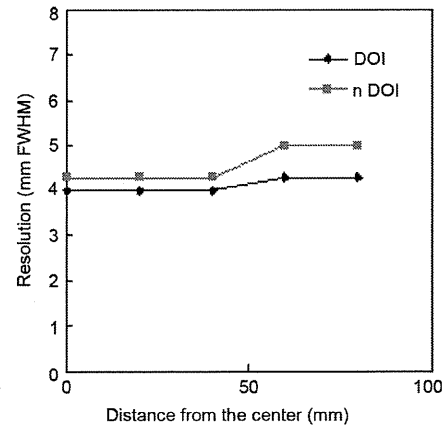Distance from the center (mm)

Fig. 7. Transaxial resolution as a function of distance from center.

The separation is good enough to divide each GSO scintillator using square boundaries. Fig. 6(b) shows an energy spectrum for one of the GSO scintillators in the block detector for Cs-137 gamma photons. The spectrum showed a single peak although the GSO scintillators consist of dual layer GSO with different decay times. Energy resolution was 15% full width at half maximum (FWHM).

Fig. 6(c) shows a pulse shape spectrum of one of the GSO scitnillators of the block detector for Cs-137 gamma photons. The pulse shape spectrum showed good separation of these two types of GSO with different decay times. The right peak in Fig. 6(c) is the GSO with 1.5 mol % Ce and left is the with 0.4 mol% Ce. The peak to valley (P/V) ratio among these peaks was 14. With this P/V ratio, the percent error in separation of two layers is almost zero.Fig. 6(d) shows the timing spectrum measured using a positron source between GSO block detectors. Timing resolution was 4.6 ns FWHM. The timing spectrum showed wider distribution at the bottom area so time window was set relatively wider (16 ns).

B. Performance of PET-Hat System

1) Spatial Resolution: Fig. 7 shows transaxial resolution as a function of distance from the center. Transaxial resolutions at the center of the FOV were 4.0 mm FWHM with DOI correction and 4.3 mm FWHM without DOI correction at the center of the FOV and 4.2 mm FWHM with DOI correction and 5.0 mm FWHM without DOI correction at 8 cm from the center of the FOV.

2) Axial Resolution: The axial resolution at the center of the FOV was 3.5 mm FWHM.

3) Sensitivity: Sensitivity profile as a function of the axial position is shown in Fig. 8. Sensitivity for point source was 0.72% at the center of the axial FOV. The count rate outside the axial FOV (48 mm) is from the scatter coincidence between detector blocks when the source is outside FOV.

4) Scatter Fraction: Scatter fraction as a function of slice number is shown in Fig. 9. Average scatter fraction was 0.6.

5) Count Rate Performance: Count rate characteristic is shown in Fig. 10. The maximum prompt minus delayed count rate was ∼ 12 kcps and NECR was 0.82 kcps within the measured activity range.
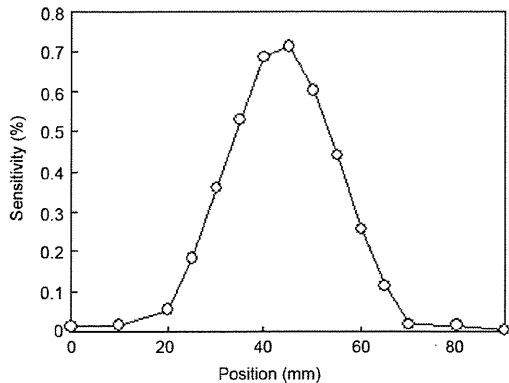
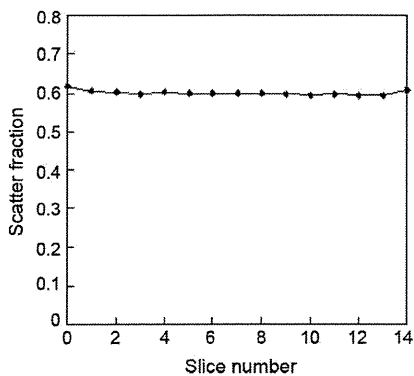Fig. 8.   Sensitivity profile as a function of the axial position.

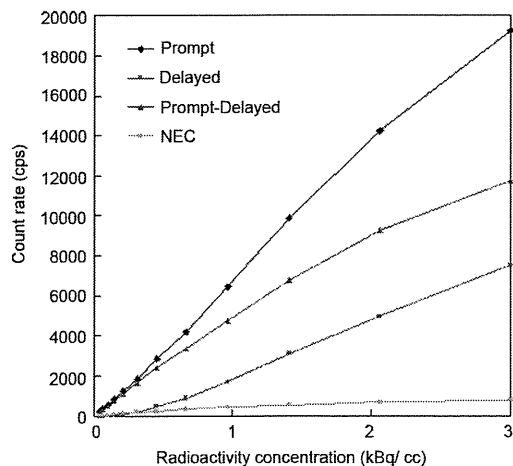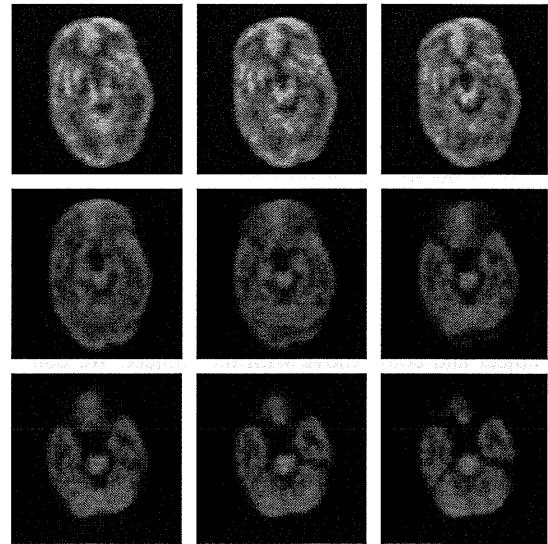Fig. 9.   Scatter fraction as a function of the slice number.

Fig. 11.   Hoffman brain phantom images contained F-18.

However the rotation or sideways neck motion produced the sift of position in the straw hat (connecting part of PET-Hat and head) that may produce image degradation from subject movements. For more free movement, rotation of the detector ring with the subject can add one more free movement of the subject with some sacrificing of the increase of the weight of the detector ring. The increase of the weight increases the inertia thus increases force for starting and stopping the movement of the detector ring.

The sensitivity of the system can be increased by several ways; increase the depth of the scintillators, use of the dense, high atomic number scintillators such as LGSO, LYSO, or LSO and increase the axial FOV. These attempts to increase the sensitivity also increase the weight of the detector ring that will require more safety mechanism for the mechanical support such as counter balanced system.

In this PET-Hat system, the effect of DOI detection was not very obvious because the depth of the GSO scintillators were relatively short, 7 mm and 8 mm. If we select GSO scitnillators with longer depth, the difference of the spatial resolution with and without DOI detection would be more attractive. However in this case, the weight of the detector ring would more heavy.

The scatter fraction of the system was relatively high, higher than the whole body PET systems [9]–[12]. The reasons are the end-shield of the detector ring is set only the lower side of the detector ring and its thickness and length are small. For the brain studies, only the scatter from the lower side of the ring will be important because there is no activity on the upper side of the detector ring. Thus the scatter contribution of the human studies will be smaller than that used NEMA phantom. The use of an additional gamma shield from the body such as gamma absorb apron may be useful for the human studies.

The image quality of the Hoffman brain phantom shown in Fig. 11 was not very attractive. One reason is the low sensitivity of the system with the small axial FOV (44 mm) and the short scintillators depth (15 mm). The other reason is the low NECR of the system because of the high scatter fraction and random

Fig. 10.   Count rate characteristic measured using 20 cm diameter, 70 cm height cylindrical phantom.

6) Images of the Hoffman Brain Phantom: Images of the Hoffman brain phantom at the central 9 slices are shown in Fig. 11. In the images we can observe the small structures of the gray matter regions of the phantom.

IV. DISCUSSION

We successfully developed a wearable brain PET system. The PET-Hat could move relatively freely with subject movement.

rate. Using the filtered back-projection for the image reconstruction is another reason of the limited quality of the phantom images. Optimization of the system parameters such as lower energy level or time window may improve the image quality in somehow. Also applying an iterative image reconstruction will improve the image quality of the PET system.

V. CONCLUSION

We have successfully developed the PET-Hat for brain research. The PET-Hat could be measured in the sitting position of the subject and could move with the subject. We conclude that the PET-Hat is promising, low cost, small size, wearable brain PET system for brain functional studies.

ACKNOWLEDGMENT

REFERENCES

[1] P. T. Fox, M. A. Mintun, M. E. Raichle, F. M. Miezin, J. M. Allman, and D. C. Van Essen, "Mapping human visual cortex with positron emission tomography," *Nature*, vol. 323, pp. 806–809, Oct. 1986.

[2] S. E. Petersen, P. T. Fox, A. Z. Snyder, and M. E. Raichle, "Activation of extrastriate and frontal cortical areas by visual words and word-like stimuli," *Science*, vol. 249, no. 4972, pp. 1041–1044, 1990.

[3] M. Corbetta, F. M. Miezin, S. Dobmeyer, G. L. Shulman, and S. E. Petersen, "Attentional modulation of neural processing of shape, color and velocity in humans," *Science*, vol. 248, no. 4962, pp. 1556–1559, 1990.

[4] P. T. Fox, M. E. Mintun, M. E. Raichle, and P. P. Herscovitch, "A noninvasive approach to quantitative functional brain mapping with H2 (15)O and positron emission tomography," *J. Cereb. Blood Flow Metab.*, vol. 4, no. 3, pp. 329–333, 1984.

[5] S. Ogawa, T. M. Lee, A. R. Kay, and D. W. Tank, "Brain magnetic resonance imaging with contrast dependent on blood oxygenation," *Proc. Natl. Academy Sciences USA*, vol. 87, no. 24, pp. 9868–9872, 1990.

[6] S. Ogawa, T. M. Lee, and G. Barrere, "The sensitivity of magnetic resonance image signals of a rat brain to changes in the cerebral venous blood oxygenation," *Magn. Reson. Med.*, vol. 29, no. 2, pp. 205–210, 1993.

[7] I. Eshed, C. E. Althoff, B. Hamm, and K. G. Hermann, "Claustrophobia and premature termination of magnetic resonance imaging examinations," *J. Magn. Reson. Imag.*, vol. 26, no. 2, pp. 401–404, 2007.

[8] S. Thorpe, P. M. Salkovskis, and A. A. Dittner, *Magn. Reson. Imag. Claustrophobia in MRI: The Role of Cognitions*, vol. 26, no. 8, pp. 1081–1088, 2008.

[9] M. Teräs, T. Tolvanen, J. J. Johansson, J. J. Williams, and J. Knuuti, "Performance of the new generation of whole-body PET/CT scanners: Discovery STE and discovery VCT," *Eur. J. Nucl. Med. Mol. Imag.*, vol. 34, no. 10, pp. 1683–1692, 2007.

[10] K. Matsumoto *et al.*, "Performance characteristics of a new 3-dimensional continuous-emission and spiral-transmission high-sensitivity and high-resolution PET camera evaluated with the NEMA NU 2-2001 standard," *J. Nucl. Med.*, vol. 47, no. 1, pp. 83–90, 2006.

[11] S. Surti, A. Kuhn, M. E. Werner, A. E. Perkins, J. Kolthammer, and J. S. Karp, "Performance of philips gemini TF PET/CT scanner with special consideration for its time-of-flight imaging capabilities," *J. Nucl. Med.*, vol. 48, no. 3, pp. 471–480, 2007.

[12] G. Brix *et al.*, "Performance evaluation of a whole-body PET scanner using the NEMA protocol. National electrical manufacturers association," *J. Nucl. Med.*, vol. 38, no. 10, pp. 1614–1623, 1997.

[13] T. Oohasi *et al.*, "In audible high-frequency sound affect brain activity: Hypersonic effect," *J. Neuriphysiol.*, vol. 83, no. 6, pp. 2548–2558, 2000.

[14] J. S. Karp, S. Surti, M. E. Daube-Witherspoon, R. Freifelder, C. A. Cardi, L. E. Adam, K. Bilger, and G. Muehllehner, "Performance of a brain PET camera based on anger-logic gadolinium oxyorthosilicate detectors," *J. Nucl. Med.*, vol. 44, no. 8, pp. 1340–1349, 2003.

[15] H. W. de Jong, F. H. van Velden, R. W. Kloet, F. L. Buijs, R. Boellaard, and A. A. Lammertsma, "Performance evaluation of the ECAT HRRT: An LSO-LYSO double layer high resolution, high sensitivity scanner," *Phys. Med. Biol.*, vol. 52, no. 5, pp. 1505–1526, 2007.

[16] E. Yoshida *et al.*, "Design and inital evaluation of a 4-layer DOI-PET system: The jPET-D4," *Igaku Butsuri.*, vol. 26, no. 3, pp. 131–140, 2006.

[17] D. L. Bailey, T. Jones, T. J. Spinks, M. C. Gilardi, and D. W. Townsend, "Noise equivalent count measurements in a neuro-PET scanner with retractable septa," *IEEE Trans. Med. Imag.*, vol. 10, no. 3, pp. 256–260, 1991.

[18] M. Watanabe *et al.*, "A new high-resolution PET scanner dedicated to brain research," *IEEE Trans. Nucl. Sci.*, vol. 49, no. 3, pp. 634–639, Jun. 2002.

[19] S. Yamamoto and H. Ishibashi, "A GSO depth of interaction detector for PET," *IEEE Trans. Nucl. Sci.*, vol. 45, no. 3, pp. 1078–1082, Jun. 1998.

[20] S. Yamamoto, "A dual layer DOI GSO block detector for a small animal PET," *Nucl. Instrum. Methods Phys. Res. A*, vol. A598, pp. 480–484, 2008.

[21] R. Pani, M. N. Cinti, R. Pellegrini, C. Trotta, G. Trotta, L. Montani, S. Ridolfi, F. Garibaldi, R. Scafè, N. Belcari, and A. D. Guerra, "Evaluation of flat panel PMT for gamma ray imaging," *Nucl. Instrum. Methods Phys. Res. A*, vol. A504, pp. 262–268, 2003.

[22] S. Yamamoto, H. Mashino, H. Kudo, K. Matsumoto, and M. Senda, "A dual layer GSO PET system for small animal: K-PET II," *IFMBE Proc.*, vol. 14, pp. 1712–1715, 2007.

[23] S. Yamamoto, "Optimization of the integration time of pulse shape analysis for dual layer detector with different amount of Ce," *Nucl. Instrum. Methods Phys. Res. A*, vol. A587, pp. 319–323, 2008.

[24] M. E. Daube-Witherspoon *et al.*, "PET performance measurements using the NEMA NU 2-2001 standard," *Nucl. Med.*, vol. 43, no. 10, pp. 1398–1409, 2002.

[25] E. J. Hoffman, P. D. Cutler, W. M. Digby, and C. J. Mazziotta, "3-D phantom to simulate cerebral blood flow and metabolic images for PET," *IEEE Trans. Nucl. Sci.*, vol. 37, no. 2, pp. 616–620, Apr., 1990.

Time course and spatial distribution of fMRI signal changes during single-pulse transcranial magnetic stimulation to the primary motor cortex

H. Shitara [a,b], T. Shinozaki [b], K. Takagishi [b], M. Honda [a], T. Hanakawa [a,c,*]

[a] Department of Functional Brain Research, National Institute of Neuroscience, National Center of Neurology and Psychiatry, Japan
[b] Department of Orthopedic Surgery, Gunma University Graduate School of Medicine, Japan
[c] PRESTO, Japan Science and Technology Agency, Japan

ABSTRACT

Simultaneous transcranial magnetic stimulation (TMS) and functional magnetic resonance imaging (fMRI) may advance the understanding of neurophysiological mechanisms of TMS. However, it remains unclear if TMS induces fMRI signal changes consistent with the standard hemodynamic response function (HRF) in both local and remote regions. To address this issue, we delivered single-pulse TMS to the left M1 during simultaneous recoding of electromyography and time-resolved fMRI in 36 healthy participants. First, we examined the time-course of fMRI signals during supra- and subthreshold single-pulse TMS in comparison with those during voluntary right hand movement and electrical stimulation to the right median nerve (MNS). All conditions yielded comparable time-courses of fMRI signals, showing that HRF would generally provide reasonable estimates for TMS-evoked activity in the motor areas. However, a clear undershoot following the signal peak was observed only during subthreshold TMS in the left M1, suggesting a small but meaningful difference between the locally and remotely TMS-evoked activities. Second, we compared the spatial distribution of activity across the conditions. Suprathreshold TMS-evoked activity overlapped not only with voluntary movement-related activity but also partially with MNS-induced activity, yielding overlapped areas of activity around the stimulated M1. The present study has provided the first experimental evidence that motor area activity during suprathreshold TMS likely includes activity for processing of muscle afferents. A method should be developed to control the effects of muscle afferents for fair interpretation of TMS-induced motor area activity during suprathreshold TMS to M1.

© 2011 Elsevier Inc. All rights reserved.

Introduction

Transcranial magnetic stimulation (TMS) is now widely applied to basic and clinical studies in neuroscience. However, the mechanisms of how TMS influences behavior are not completely clear. It is conceivable that TMS most strongly influences neural activity beneath the TMS coil, but it has been proven that TMS can also modulate neural activity in the remote regions (Paus et al., 1997). Advance in technology now allows for combining TMS and functional magnetic resonance imaging (fMRI), which can measure locally and remotely induced activity changes in the whole brain (Bestmann et al., 2003; Bohning et al., 1998; Hanakawa et al., 2009).

Previous TMS-fMRI studies have measured TMS-induced changes of blood-oxygenation level-dependent (BOLD) signals, which are widely used as a surrogate marker of the summation of synaptic/neuronal activity. The BOLD contrast reflects hemodynamic changes involving a

complex interaction between levels of oxygenation, blood flow and blood volume (Nair, 2005; Wang et al., 2004). The coupling mechanisms of synaptic/neuronal activity and BOLD signals remain ambiguous although BOLD signals show reasonable correlation with synaptic and neuronal activities measured with electrophysiological methods (Logothetis, 2000; Ogawa et al., 2000). Notably, recent studies have shown that TMS may change cerebrovascular reactivity (Rollnik et al., 2002; Sallustio et al., 2010). Since the sympathetic nervous system regulates reactivity of the cerebral vasculature, possible interference of TMS with sympathetic regulation may explain this finding. Alternatively, TMS could disrupt functions of the local circuitry consisting of interneurons and astrocytes, regulating dilation of arterioles (Zonta et al., 2003). Since TMS would most strongly influence the region beneath the coil, we cannot exclude the possibility that TMS may particularly affect the neurovascular coupling of the stimulated site. Previously, near-infrared spectroscopy (NIRS) was applied to examine the time-course of hemodynamic signal changes following single-pulse TMS. One study reported increases in oxyhemoglobin after both single-pulse TMS and voluntary movement (Noguchi et al., 2003) while another one found marked decreases in deoxyhemoglobin without increases in oxyhemoglobin and total hemoglobin (Mochizuki

* Corresponding author at: Department of Functional Brain Research, National Institute of Neuroscience, National Center of Neurology and Psychiatry, 4-1-1 Ogawahigashi, Kodaira 187-8502, Japan.
E-mail address: hanakawa@ncnp.go.jp (T. Hanakawa).

et al., 2006). This discrepancy may partly stem from the possible disruption of hemodynamic responses during TMS.

Previous TMS-fMRI studies applying TMS to the primary motor cortex (M1) consistently reported activity in local and remote motor areas during TMS. Intriguingly, the directly stimulated M1 shows significantly increased activity only with stimulation above the level of resting motor threshold (RMT) whereas the remote motor areas including the supplementary motor areas (SMA) showed significant activity below the RMT (Bestmann et al., 2003; Fox et al., 2006; Hanakawa et al., 2009; Speer et al., 2003). It remains unknown why remote motor areas show blood flow changes at lower stimulation intensities than does the M1 on which TMS should exert a direct impact. This paradox could at least in part result from the fact that the previous TMS-fMRI studies employed standard hemodynamic response functions (HRF) to detect BOLD signal changes. That is, the profile of BOLD signal changes in M1 beneath the TMS coil could differ from that in remote motor areas because of the possible disruption of normal neurovascular coupling.

In the present study, we conducted an fMRI experiment to characterize the time-course and spatial distribution of BOLD signal changes evoked by TMS in the motor areas. Previous research has described the time-course of TMS-evoked activities using a block-design fMRI (Bestmann et al., 2004; Bohning et al., 1999), which precludes a fine analysis of the signal time-course in response to each stimulus. The primary purpose of the present study was thus to examine time-course of fMRI signal changes following single-pulse TMS with a finer temporal resolution than ever. This knowledge should provide an important basis to justify the comparison of the spatial distribution of fMRI activity during TMS with that during other tasks shown to induce HRF-compatible fMRI signal changes. After gaining knowledge on the time-course of TMS-induced activity, we then compared the spatial distribution of activity during single-pulse TMS with that during motor and somatosensory reference conditions. The reference conditions included cued voluntary movement and electrical median nerve stimulation (MNS), both of which involved the same effector with the TMS. The findings suggested the effects of muscle afferents onto motor area activity during suprathreshold TMS to the M1.

Experimental procedures

Subjects

Thirty-six healthy adults (mean age = 27.0 years; range 20–46 years) participated in the present experiment. None of the participants reported any history of neuropsychiatric disorders, including epilepsy. All participants were right handed. The review board of the National Center of Neurology and Psychiatry approved the study protocol. The subjects were fully informed about the experimental procedure, and all gave written informed consent prior to participation.

Stimulation and electromyography monitoring

A 3-Tesla whole-body MRI scanner equipped with a circular polarization head coil (Siemens Magnetom Trio; Erlangen, Germany) was used for the experiment. We delivered TMS to the hand representation of the left M1 (M1-hand). The "motor hot spot" where TMS evoked a maximal motor response in the right abductor pollicis brevis (APB) muscle was identified for each participant while lying supine on the scanner bed. The APB was the primary muscle of interest in this experiment, in accord with our previous experiment (Hanakawa et al., 2009). An MRI-compatible figure-of-eight TMS coil with an outer-wing diameter of 70 mm (MR coil, Magstim, Witland, Wales, UK) was positioned tangentially to the scalp at the "motor hot-spot". The orientation of the TMS coil was approximately 45° from the medial-

lateral axis. The TMS coil was connected to a stimulator (SuperRapid, Magstim, Witland, Wales, UK) via a 7-m cable running through a wave guide tube appropriate for radiofrequency wave filtering. The TMS stimulator produced biphasic electrical pulses of approximately 250-μs duration and a rise time of 50 μs.

For the MNS-fMRI experiment, electrical stimulation was delivered through a pair of MRI-compatible electrodes (Nihon Kohden, Tokyo, Japan). The electrodes were connected to an electric current stimulator (Nihon Kohden, Tokyo, Japan) placed outside the scanner room. The maximum stimulator output was 50 mV. Constant-voltage square waves with a pulse duration of 0.3 ms were applied to the right median nerve at the wrist. The sensory threshold was determined by each participant's verbal report of sensation in the first three fingers without muscle twitching. A motor threshold for eliciting APB activity was determined with EMG monitoring in each participant. No participants reported a sensation of pain. The electrical stimulation procedure did not cause any artifacts in the functional MR images.

EMG was monitored and recorded during the fMRI experiments. For EMG recording during fMRI, we used a modified version of the "stepping-stone sampling" (SSS) method (Hanakawa et al., 2009), which was originally developed for combined electroencephalography and fMRI recording (Anami et al., 2003). In 14 participants who underwent the TMS-fMRI experiment only, motor evoked potentials (MEPs) were recorded from the right APB and the right abductor digiti minimi (ADM) muscles using SynAmps (Neuroscan, Sterling, VA, USA). Surface electrodes with shielded plates and cables were placed over the right APB and ADM muscles with an inter-electrode distance of approximately 2 cm. In the rest of the subjects, MEPs were recorded from the bilateral APB and ADM muscles using BrainAmp ExG MR (Brain Products, Gilching, Germany). EMG signals were fed to a digital amplifier electrically through a radiofrequency filter (SynAmps) or to a battery-driven amplifier placed on the scanner bed (BrainAmp ExG MR). A ground electrode was placed on the dorsal surface of the right wrist. As the SSS method requires exact synchronization between the timing of EMG sampling and that of gradient pulses for MRI acquisition, the SynAmps amplifier was externally driven by the clock of the MRI scanner. For this purpose, the clock frequency was down-sampled from the original 10 MHz to 10 kHz using a custom-made clock divider (CD5; Physio-Tech, Tokyo, Japan). Furthermore, trigger pulses from the scanner were sent to the CD 5 clock divider to synchronize the onset of EMG measurement and MRI acquisition. For EMG recorded with BrainAmp ExG MR, the amplifier and MRI scanner were synchronized using SyncBox (Brain Products, Gilching, Germany) to receive the clock and trigger signals from the scanner. EMG data were either sampled at a digitization rate of 1 kHz with an amplitude resolution of 0.336 μV/bit and a dynamic range of 22 mV (SynAmps), or a digitization rate of 5 kHz with an amplitude resolution of 0.5 μV/bit and a dynamic range of 16 mV (BrainAmp ExG MR). The data sampled with BrainAmp ExG MR were down-sampled from 5 kHz to 1 kHz to match the sampling rate of the data from SynAmp at a later processing stage.

Isometric contraction was employed for all types of movements in the present experiment. Custom-made, non-magnetic splints covering the hand, wrist and elbow joints were used to restrict the movement of the upper limbs on both sides. Then, both upper limbs were tightly fixed with elastic bandages and taped onto the splints. The setup was intended to minimize joint movements, and the effects of antagonistic muscles due to stretching. In addition, the fixation of the hand position should minimize changes of EMG and the shape of imaging artifacts on EMG over time. The position of the TMS coil was adjusted while stimulation was delivered every 5 s to elicit stable production of MEPs from the right APB muscle. The TMS coil was then fixed immobile to the scanner bed with a custom-made holder made from polyetheretherke-tone plastic. Foam pads and vacuum cushions were used to minimize head motion during scanning. After the participant's head was positioned at the MRI gantry center, the RMT was defined individually